Scripta Materialia 196 (2021) 113761

Contents lists available at ScienceDirect

Scripta Materialia

journal homepage: www.elsevier.com/locate/scriptamat

A strategy to introduce gradient equiaxed grains into Zr sheet by combining laser surface treatment, rolling and annealing

Linjiang Chai[a,*], Yufan Zhu[a], Xing Hu[a], Korukonda L. Murty[b], Ning Guo[c], Liang-Yu Chen[d], Yanlong Ma[a], Lai-Chang Zhang[e]

[a] College of Materials Science and Engineering, Chongqing University of Technology, Chongqing 400054, China
[b] Department of Nuclear Engineering, North Carolina State University, Raleigh, NC 27695-7909, USA
[c] Faculty of Materials and Energy, Southwest University, Chongqing 400715, China
[d] School of Science, Jiangsu University of Science and Technology, Zhenjiang, Jiangsu 212003, China
[e] School of Engineering, Edith Cowan University, 270 Joondalup Drive, Joondalup, Perth, WA 6027, Australia

ARTICLE INFO

Article history:
Received 27 October 2020
Revised 6 January 2021
Accepted 23 January 2021

Keywords:
Laser surface treatment
Rolling and annealing
Gradient equiaxed grains
High angle boundaries
Strain induced boundary migration

ABSTRACT

A novel strategy combining laser surface treatment, rolling and annealing (LST-RA) to produce gradient equiaxed grains is proposed and verified after applying to pure Zr sheet. Dense high angle boundaries (HABs) are first produced by the laser-induced rapid $\beta \rightarrow \alpha$ transformation in the surface layer of pure Zr while a considerable amount of stored energy is then introduced by 50% rolling. During subsequent annealing, the preexisting denser HABs facilitate generating more recrystallization nuclei in the surface layer than in the matrix through the strain induced boundary migration mechanism. This eventually results in a gradient equiaxed grain structure from surface to interior of the pure Zr sheet. Furthermore, the fine-grained surface layer is found to have a weakened texture compared to the coarse-grained matrix.

Gradient materials are a group of materials that exhibit spatial gradients in local chemical composition, phase constitution or grain size [1-3]. In recent years, the introduction of a structural gradient has been demonstrated to be capable of overcoming property limitations of conventional metallic materials with homogeneous or random microstructures [4-7]. Specifically, gradient grains are noted to effectively alleviate stress concentrations during loading leading to exceptional strength-ductility synergy. There have been several strategies explored by earlier researchers to prepare gradient grain structures, namely surface mechanical attrition treatment [5,7], surface mechanical grinding treatment [8,9] and repeated torsion [6,10]. Such strategies work mainly by introducing plastic deformation to different extents from surface to interior of metallic materials to generate grain-size gradients. However, ultrahigh-density deformation defects usually exist in as-such processed surface layers leading to lamellar shaped (non-equiaxed) fine grains. Subsequent annealing results in rapid recrystallization with grain coarsening in these fine-grained surface layers, leading to coarse grains comparable to or even coarser than those in the interior region [11]. One could expect greatly improved structural stability if there is a strategy to prepare gradient structures with defectless equiaxed grains in both the surface and the interior regions. Recrystallization annealing is well known as an effective means to reduce structural defects in deformed metals. Sizes of recrystallized grains are largely determined by their nucleation behaviors that prefer to proceed at sites near high angle boundaries (HABs) [12]. Denser preexisting HABs facilitate generating more nuclei that could subsequently develop to be finer grains. This suggests that introducing HABs with varied densities from surface to interior might be a key to produce gradient equiaxed grains during annealing.

Laser surface treatment (LST) has been well accepted as a feasible and effective surface modification method for many metallic materials [13,14]. Interestingly, our recent work [15,16] demonstrated that the LST was able to produce high-density HABs in the surface layer of Zr alloys along with microstructural refinement. Hence, in the present work, we design a novel strategy combining LST, rolling and annealing (LST-RA) to produce gradient equiaxed grain structures in pure Zr.

The as-received material was a fully recrystallized pure Zr sheet with impurities of ~1.15 wt.% Hf, ~0.15 wt.% O and <0.08 wt.% Fe+Cr. Rectangular specimens with dimensions of 18, 12 and 2 mm along rolling, transverse and normal directions (denoted as RD, TD and ND, respectively) were cut from the as-received sheet. After surface cleaning, their RD-TD surfaces (both front and back

* Corresponding author.
E-mail address: chailinjiang@cqut.edu.cn (L. Chai).

https://doi.org/10.1016/j.scriptamat.2021.113761
1359-6462/

Table. 1
Processing parameters of the employed LST.

Parameters	Values
Laser power (W)	36
Scanning speed (mm•s^{-1})	3
Defocusing amount (mm)	+2
Peak power (kW)	1
Pulse duration (ms)	6
Frequency (Hz)	6
Power density (W•mm^{-2})	45.9
Linear energy density (J•mm^{-1})	12
Beam diameter (mm)	1
Overlap (%)	50

sides) were subjected to LST along RD in a pulsed laser device (600W Nd:YAG) with processing parameters shown in Table 1. Subsequently, the LSTed sheet was rolled at room temperature by 5% per pass to a thickness reduction of 50% (denoted as LST-R) and then annealed at 550°C for 1 h in a box furnace (denoted as LST-RA). A schematic of these processing steps can be found in Fig. S1. Electron channel contrast (ECC) imaging and electron backscatter diffraction (EBSD) techniques in a Zeiss Sigma HD field emission gun scanning electron microscope (FEGSEM) were then utilized to perform microstructural characterizations. The EBSD system consisted of a NordlysMax^2 detector (Oxford Instruments) with Aztec 2.4 and HKL Channel 5 software packages used for data acquisition and post-processing analyses, respectively. Before ECC and EBSD examinations, the to-be-analyzed surfaces (RD-ND plane) were mechanically ground using SiC abrasive paper (3000# in the final step) and then electro-polished in a mixture of 10 mL perchloric acid, 20 mL butyl cellosolve and 70 mL methanol at 20 V and -30°C for 40 s.

Cross-sectional views of microstructures in the LSTed specimen are included in Fig. 1. Distinct from its matrix composed of equiaxed grains with relatively uniform sizes (8.5 ± 4.7 μm), Fig. 1a and b show that its surface layer (~200 μm in depth) is comprised of α plates in either parallel or interlaced form (mean plate width 1.1 ± 1.0 μm). Further observation reveals ultra thin twins (<100 nm) inside some plates (as arrowed in Fig. 1b), suggesting them to be twinned martensite produced by rapid $\beta \rightarrow \alpha$ transformation [15,17]. From Fig. 1a and c, a transition layer is observable between the surface layer and the matrix. It has the layer thickness of ~120 μm with mixed plates and bulk grains, corresponding to transformation microstructures after cooling from $\alpha+\beta$ domains [18]. EBSD characterization for a typical laser-modified region (including both the surface and the transition layers) is displayed in Fig. 1d, revealing high-density HABs separating fine plates as well as gradually changed grain structures [15]. Such gradient structures should be related to temperature gradients produced in the LST, as revealed by numerical simulation (Fig. S2). Fig. 1e presents a misorientation angle distribution (MAD) histogram corresponding to the boxed region E in Fig. 1d, indicating that the majority of misorientations have high angles concentrated on ~60°. Meanwhile, there also exist two minor misorientation peaks around 10° and 90°. According to the Burgers orientation relationship (OR) ($\{0001\}_\alpha // \{110\}_\beta$ and $<11\bar{2}0>_\alpha // <111>_\beta$) [19], five possible misorientations can be produced between any two of α orientations transformed from one β orientation, namely 10.5°/ < 0001 >, 60°/ < 11$\bar{2}$0 >, 60.8°/ < 1 1.38$\bar{2}$.38$\bar{0}$0.36 >, 63.3°/ < 5 5$\bar{1}$0 3 > and 90°/ < 1 1.38$\bar{2}$.38 0 > (the last four belonging to high angle misorientations) [20]. After further analyzing rotation axes of specific misorientations (Fig. 1e), they are found to be consistent with those Burgers misorientations. When the pure Zr specimen is irradiated by the pulsed laser beam, a layer of material near its surface will be rapidly heated to induce $\alpha \rightarrow \beta$ transformation. As the pulse duration is very short, sufficient

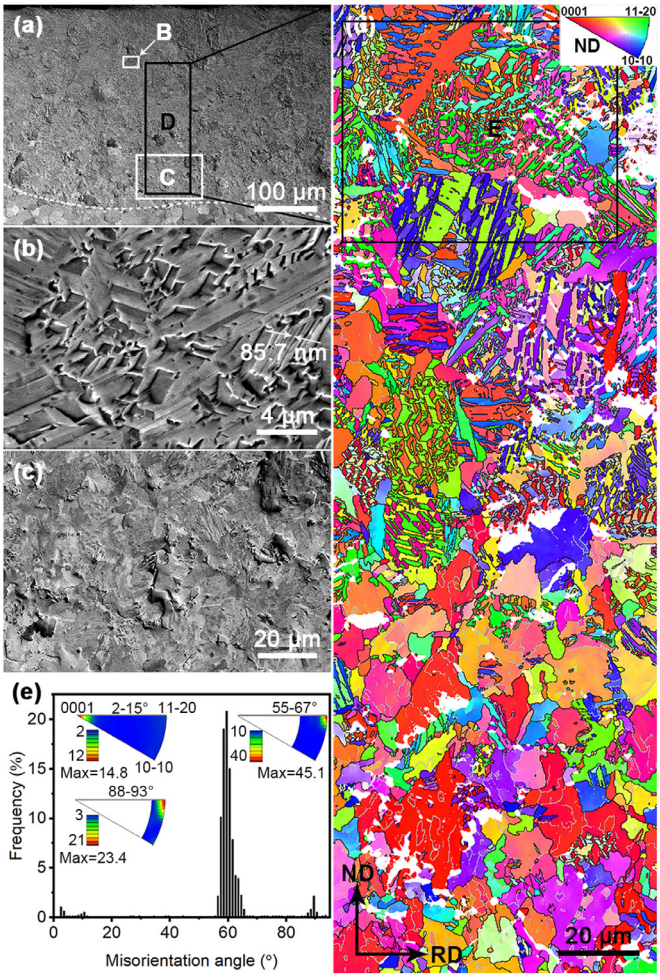

Fig. 1. Microstructural characteristics of the LSTed specimen: (a) ECC image at low magnification; (b) magnified region B in (a); (c) magnified region C in (a); (d) EBSD IPF map (step size 0.2 μm) with black and silver lines representing HABs and LABs, respectively; (e) MAD histogram corresponding to region E in (d). Dashed lines in (a) roughly distinguish laser-modified regions and the matrix.

heat extraction through the cold matrix ("self-quenching") occurs leading to ultrafast $\beta \rightarrow \alpha$ cooling [16]. This produces fine plates (martensite) in the surface layer of the LSTed specimen, and the obedience of Burgers OR during phase transformation gives rise to dense HABs. Similar grain boundary distribution characteristics have also been observed in many Zr alloys after rapid β quenching [21,22].

Fig. 2 presents microstructures of both the surface layer and the matrix of the LST-Red specimen and a large number of low angle boundaries (LABs) appear inside both plate structures of the surface layer and bulk grains of the matrix (Fig. 2a and b) suggesting the introduction of high stored energy into both of them by the 50% rolling. Meanwhile, the area density of HABs (2.69 μm^{-1}) is significantly higher than that in the matrix (0.31 μm^{-1}). Fig. 2c and d are kernel average misorientation (KAM) maps revealing microstrains and stored energy in metals [23-25]. Average KAM values of the surface layer and the matrix are 2.05° and 2.04°, respectively, markedly higher than that of the as-received material (0.24°) indicating a similar amount of stored energy accumulated inside them during rolling. From MAD histograms in Fig. 2e and f, the fraction of HABs in the surface layer (44.65%) is found to be higher than that in the matrix (15.27%) consistent with those revealed by IPF maps (Fig. 2a and b). Thus much denser HABs are retained in the surface layer of the LST-Red specimen that are expected to play an important role during subsequent recrystallization.

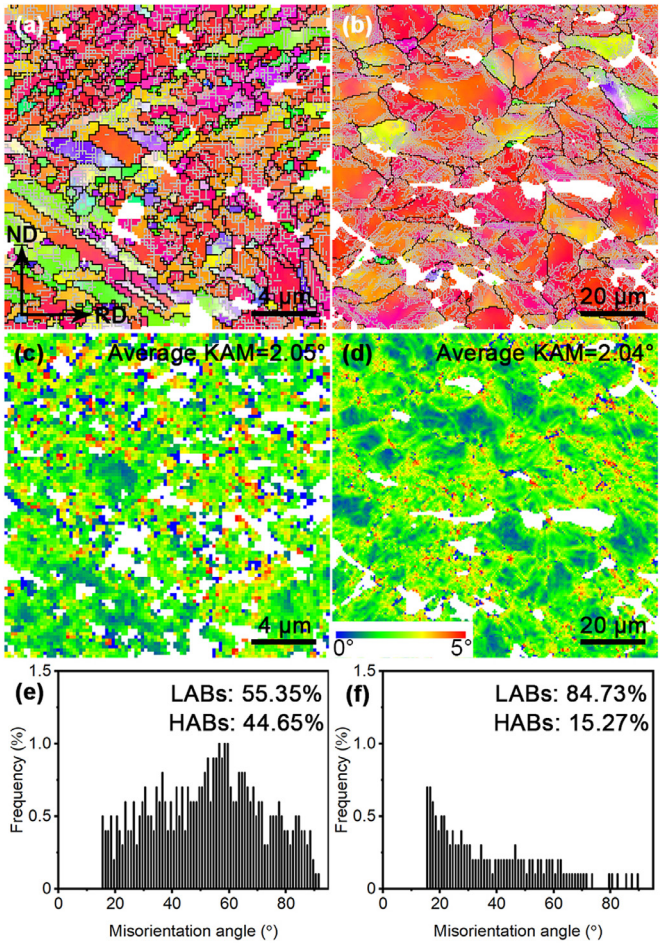

Fig. 2. Microstructural characteristics of the LST-Red specimen: (a, c and e) EBSD IPF map (step size 0.2 μm), KAM map and MAD histogram in the surface layer, respectively; (b, d and f) EBSD IPF map (step size 0.5 μm), KAM map and MAD histogram in the matrix, respectively. The color codes in (a and b) are the same as that in Fig. 1d.

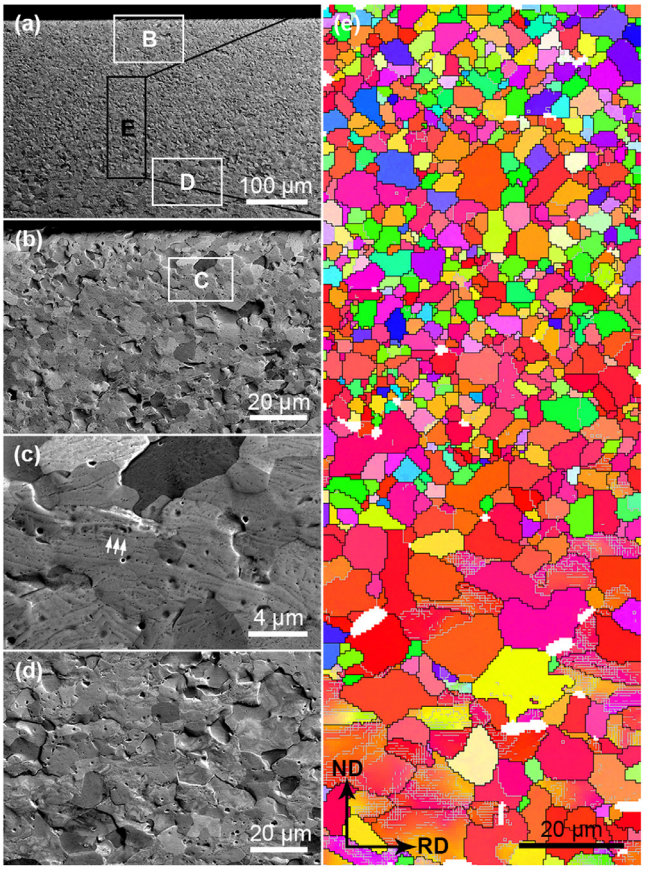

Fig. 3. Microstructural characteristics of the LST-RAed specimen: (a) ECC image at low magnification; (b) magnified region B in (a); (c) magnified region C in (b), with arrows indicating fine SPPs; (d) magnified image of region D in (a); (e) EBSD IPF map (step size 0.5 μm) with the same color code as that in Fig. 1d.

Microstructural characteristics of the LST-RAed specimen are shown in Fig. 3, revealing gradient equiaxed grains with sizes gradually increasing from the surface to the interior. Fig. 3b shows that the prior plate structures in the surface layer are completely replaced by recrystallized structures (near-equiaxed grains) with some second phase particles (SPPs) distributed linearly inside these recrystallized grains. Such microstructural feature was earlier observed in a β-quenched and recrystallization annealed Zr alloy attributed to preferential precipitation of supersaturated alloying elements (Fe and Cr) along plate boundaries [26]. Most grains in the matrix also have near-equiaxed morphology (Fig. 3d) and a gradient distribution of grain sizes is presented from surface to interior of the LST-RAed specimen (Fig. 3e). Quantitatively, the average grain size in the top surface is 2.7 ± 1.8 μm that becomes much larger in the matrix (5.3 ± 2.9 μm), and a gradual increase in grain size between them can be observed (see Fig. S3 for more results).

Sizes of recrystallized grains are known to mainly depend on nucleation density and growth rate with the latter essentially determined by stored energy introduced by prior deformation. The surface layer and the matrix in the LST-Red specimen have very close KAM values (Fig. 2c and d) indicating hardly any differences in stored energy between them. This suggests that different grain sizes should be ascribed to varied densities of recrystallization nuclei in these regions since recrystallization nucleation often closely relates to preexisting HABs. When there is considerable difference in dislocation density on the two sides of a HAB, it tends to bulge into the side with higher stored energy (dislocation density) until recrystallization nuclei with stable sizes are formed. Such recrystallization mechanism is termed as the strain induced boundary migration (SIBM) and has been verified to be the primary controlling mechanism in Zr alloys deformed slightly or moderately (like 50%-rolled) [27,28]. As HABs are preferred sites for nucleation in this process, denser preexisting HABs must result in more recrystallization nuclei [12]. Fig. 2a and b show a higher density of HABs in the surface layer than in the matrix, suggesting denser nuclei to be generated near the surface at the early stage of recrystallization annealing. These nuclei initially grow rapidly driven by stored energy. However, once they meet other recrystallized grains, the driving force of boundary migration would be greatly reduced leading to suppressed growth [29]. For the LST-RAed specimen, recrystallization nuclei with varied densities in different regions gradually develop to yield gradient equiaxed grain structures, i.e. fine grains in the surface layer and coarse grains in the matrix.

Pole figures of various specimens/regions are presented in Fig. 4, which are derived from EBSD datasets with the same scanning area (including thousands of grains) to insure reliable textural comparisons. Fig. 4a shows that the as-received specimen has a typical bimodal basal texture with the basal maxima (5.5 times of random) tilted about ±20-40° from the ND toward the TD [30]. Meanwhile, $< 10\bar{1}0 >$ or $< 11\bar{2}0 >$ of most of the grains are aligned close to the RD. For the LSTed specimen, however, distinct textural characteristics are observed for the surface layer, that is, considerably decreased textural intensity with largely scattered ori-

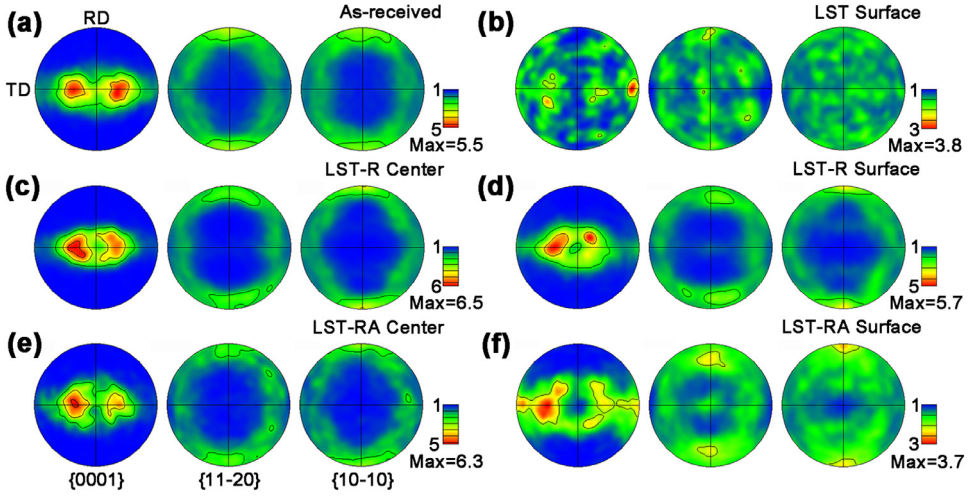

Fig. 4. Pole figures of (a) the as-received specimen and (b) the surface layer of the LSTed specimen, (c and d) matrix and surface layer of the LST-Red specimen, and (e and f) matrix and surface layer of the LST-RAed specimen, with each one calculated using EBSD dataset with scanning area larger than 0.5 mm^2.

entations (Fig. 4b). Such changes should be related to the presence of multiple variants generated by rapid $\alpha \rightarrow \beta \rightarrow \alpha$ transformation (high heating/cooling rates help suppress variant selection) [31]. Fig. 4c reveals that the initial texture is well maintained in the matrix of the LST-Red specimen except for a slightly intensified $< 10\bar{1}0 >$ //RD component, consistent with typical rolling textures of Zr alloys [32]. For the surface layer of the LST-Red specimen (Fig. 4d), however, the 50% rolling makes c-axes of most grains to be aligned near the ND (ring-like distribution), with the $< 10\bar{1}0 >$ //RD component intensified as well. Previous studies [30,33] demonstrated that during rolling at room temperature, twinning was difficult to be activated in pure Zr sheet with a typical bimodal basal texture and plastic strains could only be accommodated by slip (prismatic, basal and pyramidal). In the present work, the microstructural characteristics revealed in Fig. 2 suggest textural characteristics of both the surface layer and the matrix of the LST-Red specimen also result from active slip. After annealing at 550°C for 1 h, no considerable textural changes are found for the matrix (Fig. 4e). In contrast, the textural intensity of the surface layer is significantly decreased, with c-axes of most grains distributing on the ND-TD plane and the $< 10\bar{1}0 >$ //RD component retained. An important feature of the SIBM mechanism is that new recrystallized grains often inherit prior orientations present in deformed structures [12,34], which explains the textural similarity of the matrix before and after annealing (Fig. 4c and e). For the surface layer, however, greatly scattered orientations are produced by the LST. Although the 50% rolling produces some preferred orientations, there are still many more scattered orientations in the surface layer compared to those in the matrix. As a result, the SIBM mechanism allows new recrystallized grains to have more orientations in the surface layer during subsequent annealing giving rise to a more scattered and weaker texture.

In summary, a novel LST-RA strategy is demonstrated to be able to introduce gradient equiaxed grains into pure Zr sheet. The LST is first utilized to produce high-density HABs in the surface layer and then 50% rolling is performed to introduce stored energy. During subsequent annealing, significantly more recrystallization nuclei are generated in the surface layer due to the preexisting denser HABs. Gradient equiaxed grain structures with grain sizes increasing from surface to interior are eventually developed. We further demonstrate that this strategy allows the surface layer to have a weaker texture than the matrix. It is anticipated that the LST-RA strategy should also be applicable to many other materials (like steels and Ti alloys) and further optimized gradient structures (Fig. S3) could be obtained after adjusting processing variables (e.g. LST parameters, rolling reduction, annealing temperature and time).

Declaration of Competing Interest

The authors declare that they have no known competing financial interests or personal relationships that could have appeared to influence the work reported in this paper.

Acknowledgments

This work was financially supported by the Fundamental and Cutting-Edge Research Plan of Chongqing (cstc2018jcyjAX0299), the University Innovation Research Group of Chongqing (CXQT20023) and the Graduate Student Innovation Program of Chongqing University of Technology (CLGYCX20202005). We also gratefully appreciate Prof. Chao Wang at Chongqing University for his assistance in numerical simulation.

Supplementary materials

Supplementary material associated with this article can be found, in the online version, at doi:10.1016/j.scriptamat.2021.113761.

References

[1] T.H. Fang, W.L. Li, N.R. Tao, K. Lu, Science 331 (2011) 1587–1590.
[2] X. Li, L. Lu, J. Li, X. Zhang, H. Gao, Nat. Rev. Mater. 5 (2020) 706–723.
[3] X. Wu, P. Jiang, L. Chen, F. Yuan, Y.T. Zhu, Proc. Natl. Acad, Sci 111 (2014) 7197–7201.
[4] E. Ma, T. Zhu, Mater. Today 20 (2017) 323–331.
[5] Z. Cheng, H. Zhou, Q. Lu, H. Gao, L. Lu, Science 362 (2018) eaau1925.
[6] Y. Wei, Y. Li, L. Zhu, Y. Liu, X. Lei, G. Wang, Y. Wu, Z. Mi, J. Liu, H. Wang, Nat. Commun. 5 (2014) 3548.
[7] K. Lu, Science 345 (2014) 1455–1456.
[8] W. L. Li, N. R. Tao, K. Lu, Scripta Mater. 59 (2008) 546-549.
[9] J. Ding, Q. Li, J. Li, S. Xue, Z. Fan, H. Wang, X. Zhang, Acta Mater. 149 (2018) 57–67.
[10] N. Guo, Z. Zhang, Q. Dong, H. Yu, B. Song, L. Chai, C. Liu, Z. Yao, M.R. Daymond, Mater. Des. 143 (2018) 150–159.
[11] R. Huang, Y. Han, J. Alloys Comp. 554 (2013) 1–11.
[12] F.J. Humphreys, M. Hatherly, Recrystallisation and related annealing phenomena, 2nd ed., Pergamon Press, Oxford, 2004.
[13] K. Xiang, L.Y. Chen, L. Chai, N. Guo, H. Wang, Appl. Surf. Sci. 517 (2020) 146214.
[14] Y. Geng, É. McCarthy, D. Brabazon, N. Harrison, Surf. Coat. Technol. 398 (2020) 126085.
[15] L. Chai, B. Chen, S. Wang, N. Guo, C. Huang, Z. Zhou, W. Huang, Appl. Surf. Sci. 364 (2016) 61–68.
[16] L. Chai, B. Chen, S. Wang, Z. Zhou, W. Huang, Mater. Charact. 110 (2015) 25–32.

[17] D. Kerr, C. Cochrane, M.R. Daymond, Metall. Mater. Trans. A 51 (2020) 2724–2737.
[18] H. Okamoto, J. Phase Equilib. Diffus. 27 (2006) 543–544.
[19] W.G. Burgers, Physica 1 (1934) 561–586.
[20] C. Chauvy, P. Barberis, F. Montheillet, Mater. Sci. Eng. A 431 (2006) 59–67.
[21] H.L. Yang, S. Kano, Y. Matsukawa, Y.F. Li, J.J. Shen, F. Li, Z.S. Zhao, Y. Satoh, H. Abe, Mater. Des. 104 (2016) 355–364.
[22] D.Leo Prakash, M. Preuss, M. Dahlbäck, J. Quinta da Fonseca, Acta Mater. 88 (2015) 389–401.
[23] Y. Wang, R. Fu, Y. Li, D. Sang, L. Jing, Mater. Sci. Eng. A 744 (2019) 171–181.
[24] L. Saraf, Microsc. Microanal. 17 (2017) 424–425.
[25] S.I. Wright, M.M. Nowell, D.P. Field, Microsc. Microanal. 17 (2011) 316–329.
[26] L. Chai, B. Luan, K.L. Murty, Q. Liu, Acta Mater. 61 (2013) 3099–3109.
[27] K.Y. Zhu, D. Chaubet, B. Bacroix, F. Brisset, Acta Mater. 53 (2005) 5131–5140.
[28] H.L. Yang, S. Kano, Y. Matsukawa, Y.F. Li, J.J. Shen, Z.S. Zhao, F. Li, Y. Satoh, H. Abe, Mater. Sci. Eng. A 661 (2016) 9–18.
[29] N. Dewobroto, N. Bozzolo, P. Barberis, F. Wagner, Z. Metallked 97 (2006) 826–833.
[30] L. Chai, B. Luan, D. Xiao, M. Zhang, K.L. Murty, Q. Liu, Mater. Des. 85 (2015) 296–308.
[31] L. Chai, J. Xia, Y. Zhi, K. Chen, T. Wang, B. Song, N. Guo, Mater. Chem. Phys. 213 (2018) 414–421.
[32] K.Y. Zhu, B. Bacroix, T. Chauveau, D. Chaubet, O. Castelnau, Metall. Mater. Trans. A 40 (2009) 2423–2434.
[33] S. Sahoo, V. Hiwarkar, I. Samajdar, G. Dey, D. Srivastav, R. Tiwari, S. Banerjee, Scripta Mater. 56 (2007) 963-966.
[34] N. Dewobroto, N. Bozzolo, F.Wagner P.Barberis, Mater. Sci. Forum 467-470 (2004) 453–458.